Massachusetts Institute of Technology

Transverse instability magnetic field thresholds of electron phase-space holes

I. H. Hutchinson

Plasma Science and Fusion Center, MIT, Cambridge, Massachusetts 02139, USA

A detailed comparison is presented of analytical and particle-in-cell simulation investigation of the transverse instability, in two dimensions, of initially one-dimensional electron phase-space hole equilibria. Good quantitative agreement is found between the shift-mode analysis and the simulations for the magnetic field (B) threshold at which the instability becomes overstable (time oscillatory) and for the real and imaginary parts of the frequency. The simulation B threshold for full stabilization exceeds the predictions of shift-mode analysis by 20–30%, because the mode becomes substantially narrower in spatial extent than a pure shift. This threshold shift is qualitatively explained by the kinematic mechanism of instability.

I. INTRODUCTION

An electron phase-space hole in a collisionless plasma is an isolated positive electric potential structure with trapped electron orbits on which the phase-space density is lower than for untrapped orbits. The resulting local decrease of electron charge density self-consistently sustains the enhanced potential in steady state [1–4]. Electron holes are formed during the nonlinear (electron trapping) phase of most electrostatic (Penrose) instabilities in one dimension [4]. They have also been widely observed in space plasmas since electric field sampling rates began to be fast enough to resolve the rapid passage of a hole past the spacecraft [5–17]. In multiple dimensions, electron holes are known from simulations to break up by what is called the transverse instability: growing perturbations that vary in the direction transverse to the direction of particle trapping, and observed in many studies [18–25]. Such instabilities probably determine the long-term multidimensional structure of these electrostatic solitonlike objects, and their ultimate dissipation into the background plasma. Therefore it is vital to understand the mechanisms involved and their bearing on experimental observations.

Recent theory of linear kink stability of an initially planar electron hole identified the kinematic mechanism of transverse instability at low magnetization, and confirmed it by comparison with simulation [26]. Detailed mathematical analysis also showed why instability is suppressed by a sufficiently strong magnetic field in the trapping direction (z), normal to the plane [27]. However a quantitative discrepancy of approximately a factor of 2 was noted between the magnetic field threshold calculated analytically and what is observed in PIC simulations. In simulations, full suppression of the kink instability takes approximately twice as strong a magnetic field as was found analytically in that work. The purpose of this paper is to report further investigations that now explain the prior discrepancy concerning the threshold, confirming and extending our understanding of the instability mechanisms.

To clarify what is meant by a kink, the spatial form of the instability is illustrated by the potential contours at two times during instability growth during a particle-in-cell (PIC)

simulation in Fig. 1. The initial equilibrium is independent of the transverse coordinate y, but as time passes, a growing displacement of the hole in the z direction develops, which is sinusoidal in y, and in this case oscillating in time. The two-dimensional simulation is independent of the third coordinate (x) throughout.

Two main factors in the previous assumptions and approximations are found to cause the discrepancy: (1) It was previously assumed that solutions to the analytic dispersion relation are purely growing modes whose frequency ω is pure imaginary; it turns out, in contrast, that there are overstable modes at fields a little above the threshold for stability of the purely growing modes. And (2) the analytic calculation approximates the eigenmode to be a pure "shift mode," consisting of a lateral motion independent of z; the PIC simulations show that at the highest unstable magnetic fields, the eigenmode is not a pure shift; the displacement is concentrated in the center of the hole. This effect allows the overstable modes to exist at somewhat higher fields than for pure shift modes.

The present paper draws heavily on the previous analysis, but removes the restriction to imaginary ω and gives direct comparisons with detailed simulations in the vicinity of the threshold. It does *not* address or explain the slower-growing instabilities observed in PIC simulations at high magnetic fields well above the threshold [20,21,23,25,28–30], which are associated with hole-wave coupling to long-wavelength perturbations often called streaks or whistlers.

II. ANALYTIC DISPERSION RELATION

We only summarize here the analysis that was carried out in Ref. [27], which should be consulted for the mathematical details. Ions are taken as a uniform immobile background and only electron dynamics are included. Throughout this paper dimensionless units are used with length normalized to Debye length $\lambda_D = \sqrt{\epsilon_0 T_e/n_0 e^2}$, velocity to electron thermal speeds $v_t = \sqrt{T_e/m_e}$, electric potential to thermal energy T_e/e, and frequency to plasma frequency $\omega_p = v_t/\lambda_D$ (time normalized to ω_p^{-1}). The linearized analytic treatment of electrostatic instability of a magnetized electron hole integrates Vlasov's
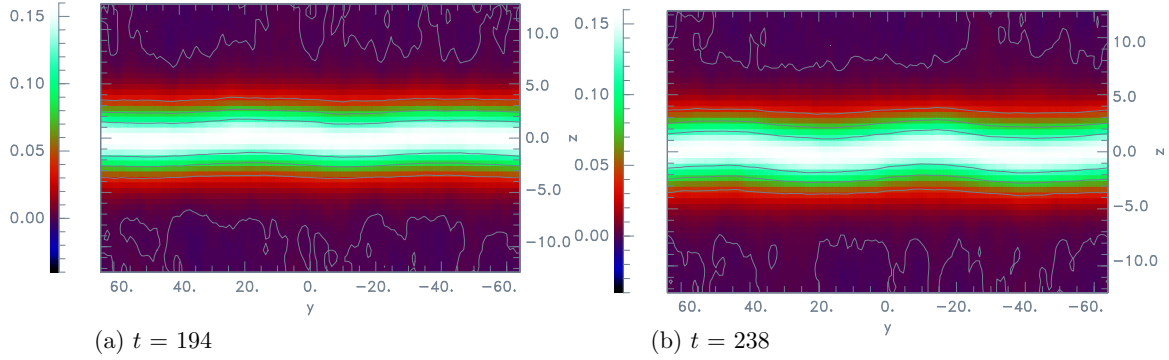
(a) $t = 194$

(b) $t = 238$

FIG. 1. Example PIC simulation of a kink instability of an initially planar hole. Contours of potential ϕ in two spatial dimensions: z is the direction of trapping and the magnetic field, y is the transverse direction. The perturbation consists of sinusoidal wave variation in the y direction of a displacement in the z direction. This case has a displacement that is a growing standing wave whose amplitude in (b) at later time $t = 238$ is opposite in sign and greater in magnitude than that in (a) at $t = 194$. ($\psi = 0.16$, $\Omega = 0.2$.)

equation along the equilibrium (zeroth order) orbits to obtain the first order perturbation to the distribution function f_1 caused by a potential perturbation ϕ_1. For an electron hole, the equilibrium is nonuniform in the (trapping) z direction and differs from the textbook wave case in that only in the transverse direction (y) does Fourier analysis yield uncoupled eigenmodes. The z dependence of the eigenmodes' potential must be expressed in a full-wave manner, so we write

$$\phi_1(\boldsymbol{x}, t) = \hat{\phi}(z) \exp i(ky - \omega t), \tag{1}$$

taking the transverse wave vector to be in the y direction without loss of generality. The integration along unperturbed

helical orbits (the characteristics of the linearized equation) gives rise to an expansion in harmonics of the cyclotron frequency ($\Omega = eB/m_e$ which represents the magnetic field strength) involving [see [27], Eq. (5.6)]

$$\Phi_m(z, t) \equiv \int_{-\infty}^{t} \hat{\phi}[z(\tau)] e^{-i(m\Omega + \omega)(\tau - t)} d\tau, \tag{2}$$

where $z(\tau) = z(t) + \int_{t}^{\tau} v_z(t') dt'$ is the position at earlier time τ. For the positive imaginary part of ω ($\omega_i > 0$) the parallel distribution function (integrated over transverse velocities) then can be found as [see [27], Eq. (5.9)]

$$f_{\parallel 1}(y, t) = q_e \phi_1(t) \frac{\partial f_{\parallel 0}}{\partial W_\parallel}\bigg|_t + \sum_{m=-\infty}^{\infty} i\left[(m\Omega + \omega) \frac{\partial f_{\parallel 0}}{\partial W_\parallel} + m\Omega \frac{f_{\parallel 0}}{T_\perp} \right] q_e \Phi_m e^{-\zeta_t^2} I_m\left(\zeta_t^2\right) e^{i(ky - \omega t)}, \tag{3}$$

where q_e and m_e are the electron charge and mass, $W_\parallel$ is the parallel energy $\frac{1}{2} m_e v_z^2 + q_e \phi$, $f_{\parallel 0}$ is the unperturbed parallel distribution function, $T_\perp$ is the perpendicular (Maxwellian) temperature, ζ_t is the transverse wave number k times the thermal Larmor radius, so that $\zeta_t^2 = k^2 T_\perp / \Omega^2 m_e$, and I_m is the modified Bessel function. The first term of this equation is the "adiabatic" contribution, which can be thought of as the perturbation that would have arisen if f had stayed the same function of energy as it was in the unperturbed equilibrium. The remaining harmonic sum is the nonadiabatic contribution we denote $\tilde{f}_\parallel$.

The specific hole equilibrium we analyze is

$$\phi_0 = \psi \operatorname{sech}^4(z/4), \tag{4}$$

where the constant ψ is the maximum hole potential: the "depth" of the hole. The corresponding trapped particle bounce time for the most deeply trapped electrons is $\omega_b = \sqrt{\psi}/2$. The background parallel velocity distribution is the Maxwellian of temperature T_e, and throughout $T_\perp = T_e$.

The main difficulty is to find the shape of the eigenfunction $\hat{\phi}(z)$ which self-consistently satisfies the Poisson equation because this is an integrodifferential eigenproblem. For slow time dependence relative to particle transit time, it can be

argued on general grounds that the eigenmode consists of a spatial shift (by small distance Δ independent of position) of the equilibrium potential profile (ϕ_0) (see [27], Sec. 3.1) giving

$$\hat{\phi} = -\Delta \frac{\partial \phi_0}{\partial z}. \tag{5}$$

We must concern ourselves with frequencies whose periods are not much longer than the transit time, so this shift form cannot be expected to hold exactly. However, we can obtain a good approximation to the corresponding eigenvalue of our system by expressing it in terms of a "Rayleigh quotient": a variational approximation which gives an eigenvalue whose errors are only second order in the deviation of the eigenmode from its exact form (a brief historical introduction can be found for example in Ref. [31]). This mathematical procedure is equivalent to requiring the conservation of total z momentum under the influence of the assumed shift eigenmode (see [27], Sec. 3). The resulting kink of the hole gives rise to two different contributions to momentum balance: F_E consists of transfer by Maxwell stress of z momentum in the y direction, and $\tilde{F}$ consists of the force exerted by the equilibrium potential on the nonadiabatic part of the charge
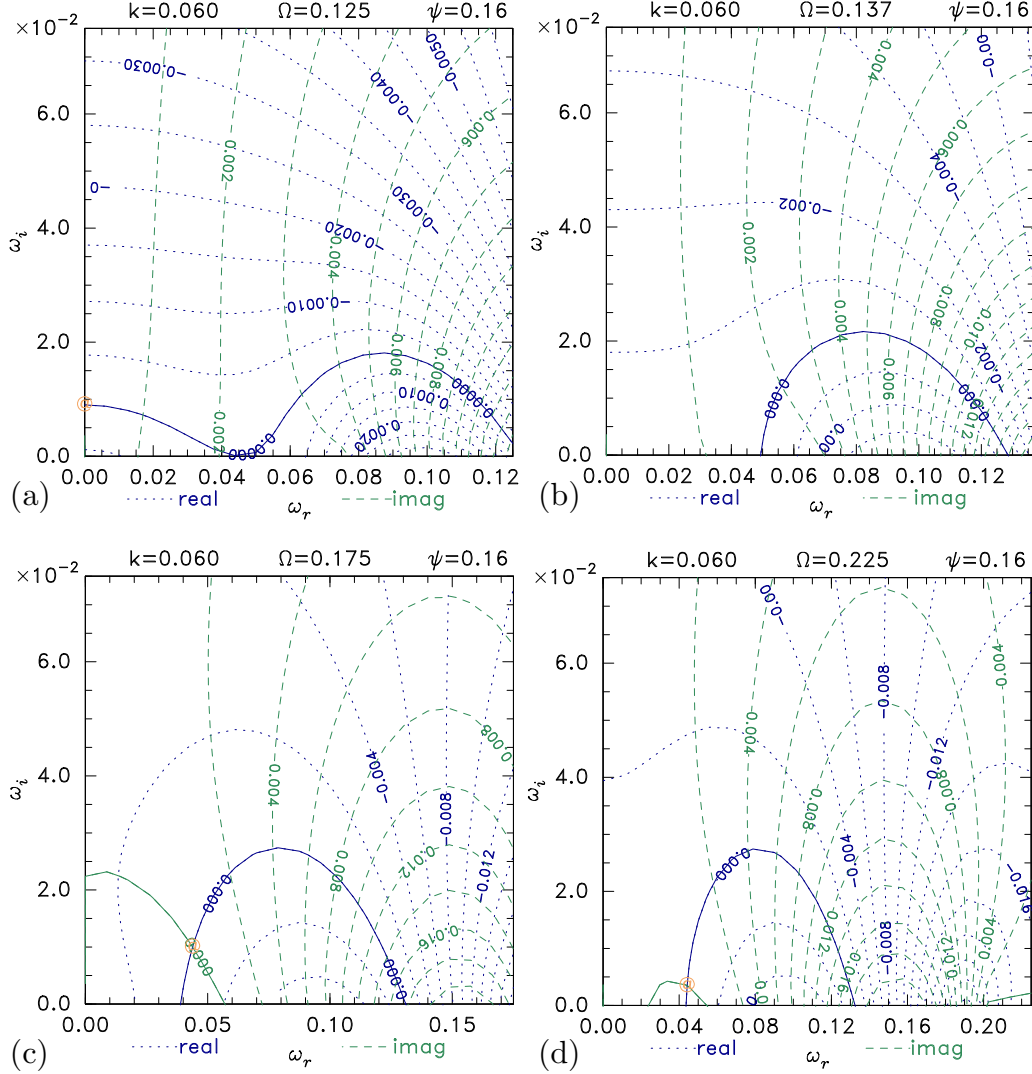
FIG. 2. Contours in the complex ω plane of the real and imaginary part of the momentum balance F_{tot}, which is required to be zero, i.e., the solution (denoted @) is the intersection of the two zero contours. (a) Purely growing case; (b) no solution; (c),(d) overstable solution. Hole parameters $\psi = 0.16$, $\omega_b = 0.2$.

density perturbation. The eigenvalue equation is that they must balance [see [27], Eq. (3.6)],

$$F_E \equiv -\epsilon_0 k^2 \int \frac{d\phi_0}{dz} \phi_1 dz = -\int \frac{d\phi_0}{dz} \left(\int q_e \tilde{f}_{\parallel} dv_z \right) dz \equiv \tilde{F},$$
(6)

into which we substitute the shift mode, Eqs. (5) and (1).

The task then, for specified real k, is to find real and imaginary parts (ω_r and ω_i) of the complex frequency that satisfy Eqs. (1)–(6). If a solution exists with positive ω_i, it is unstable; if no such solution exists, the equilibrium is stable. The integrals of Eqs. (2) and (6) are carried out numerically for given ω. Solutions are displayed graphically and found precisely by 2D Newton iteration of ω to find the roots of the complex quantity $F_{\text{tot}} = \tilde{F} - F_E$ when they exist.

III. OVERSTABILITY CALCULATED ANALYTICALLY

Figure 2 shows contours of total (complex) momentum transfer rate F_{tot} for a shift eigenmode in the complex ω

plane, for a (real) transverse wave number k chosen to give a large instability growth rate. It shows where the analytic solutions for unstable shift kinks occur. The solution of the associated dispersion relation, $F_{\text{tot}} = 0$, is at the intersection of the two zero contours, for the real and imaginary parts. In Figs. 2(a) and 2(b) the $\text{Im}(F_{\text{tot}}) = 0$ contour exists only at $\omega_r = 0$, the imaginary axis. In (a) a solution exists (with $\omega_i \simeq 0.01$) shown by the (@-denoted) convergence point of the Newton iteration. Convergence requires only a few iterations. In (b), at slightly higher field, no solution exists because the $\text{Re}(F_{\text{tot}}) = 0$ contour is absent at $\omega_r = 0$. Newton iteration takes the root search into the negative ω_i region, where the integration technique is invalid (and the mode would be damped). This instability suppression occurs at the previously documented analytic threshold $\Omega \simeq 0.68\omega_b$, which for this hole depth ($\psi = 0.16$) is $\Omega \simeq 0.136$ (ω_p units).

However, as Ω is increased further, for example Fig. 2(c), a new solution appears away from the imaginary axis, because the $\text{Im}(F_{\text{tot}}) = 0$ contour is now present at finite ω_r. This type of solution persists up to a second threshold at fields just above
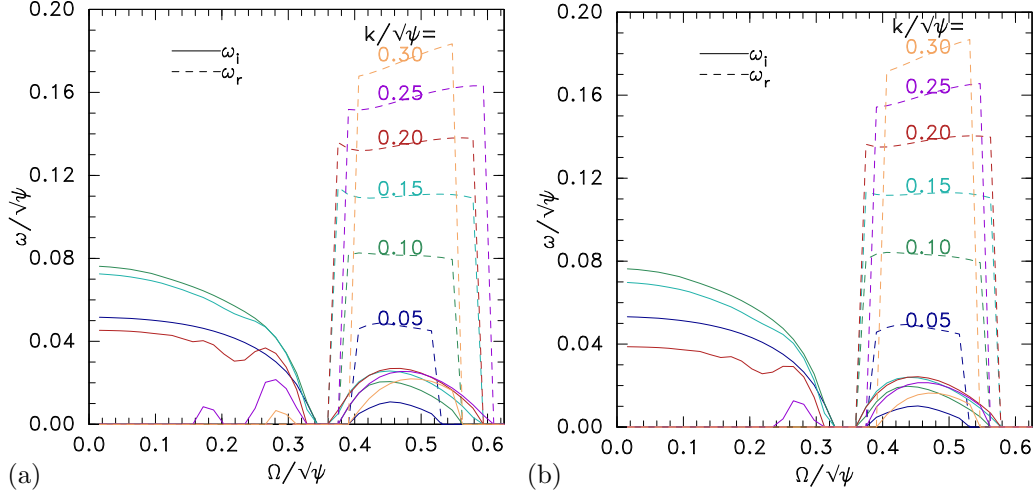
FIG. 3. Summary of dispersion solutions for (a) $\psi = 0.16$ and (b) $\psi = 0.36$, and six k values.

the case (d) when the $\mathrm{Im}(F_{\mathrm{tot}}) = 0$ contour disappears again below $\omega_i = 0$ at the relevant ω_r. The contour plot domains are deliberately chosen large to illustrate that there are no other roots. Plots like these also confirm there are no solutions at higher Ω.

The dependence of the solutions on the transverse wave number can be seen by plotting the solution ω as a function of Ω, as illustrated in Fig. 3. Here we show values normalized to $\sqrt{\psi}$ because as was noted in prior analysis this makes the curves almost independent of hole depth (at least for shallow holes). This near-universality is evident by inspection of the two cases (a) $\psi = 0.16$ and (b) $\psi = 0.36$. The purely growing mode, which exists for $\Omega/\sqrt{\psi} \lesssim 0.33$, is just what was analyzed before and the results are exactly the same. It is unstable from small k to about twice the k having maximum growth rate: $k \simeq \sqrt{\psi}/8$. Purely growing modes for all k's stabilize at $\Omega \simeq 0.33\sqrt{\psi}$. Then overstable modes (undiscovered by prior analysis) with $\omega_r \sim k$ appear at marginally higher Ω. It is uncertain, in view of rounding errors and other numerical limitations especially at high k, whether the apparent gap here between the two types of instability is really present; in any case it is narrow. The overstable mode's ω_r is essentially independent of Ω, but the growth rate has a continuous profile. The fastest growing oscillatory mode at fixed Ω has $k/\sqrt{\psi}$ value of 0.15–0.2 ($\omega_r/\sqrt{\psi} \simeq 0.11$–0.14) at the lower end of the unstable Ω range, but 0.20–0.25 ($\omega_r/\sqrt{\psi} = 0.14$–0.16) at the upper end. The latter, higher-k, modes also remain unstable to higher values of Ω, even when k values are high enough to suppress the purely growing, low-Ω, instability entirely. The fastest growth rate of the overstable mode is $\omega_i \simeq 0.025\sqrt{\psi}$.

The relationship between k and ω_r can be understood as a kink vibration of the hole (in the same spirit as was analyzed in Ref. [28] for a waterbag hole) that balances $\tilde{F}$ and F_E. Reference [27] referred to the Maxwell stress F_E as a "tension" force, but that terminology is somewhat misleading. In fact F_E is a force that acts to *increase* any kink displacement of the hole, not to *oppose* it. The vibration then occurs because $\tilde{F}$ is such as to *oppose* kinking by transferring momentum to particles ("jetting" them) in the direction of z displacement. Jetting ($\tilde{F}$) for low frequency is approximately proportional

to ω^2, that is to acceleration, while F_E is independent of ω. Therefore their roles have reversed sign in analogy with a stretched string. F_E acts like negative tension (compression) and $\tilde{F}$ acts like negative inertia. The resulting momentum balance is nevertheless a vibrating wave. A fit to the numerically calculated relationship, approximately independent of hole depth ψ, namely

$$\omega_r/\sqrt{\psi} \simeq 0.45(k/\sqrt{\psi})^{0.75}, \tag{7}$$

is shown in Fig. 4. The range of ω_r values is shown by the vertical bars.

In summary, the shift-mode analytic results show there are two threshold values of magnetic field. The purely growing mode is suppressed for $\Omega \gtrsim 0.34\sqrt{\psi} \simeq 0.68\omega_b$. The overstable mode appears immediately above this threshold and is present until $\Omega \gtrsim 0.6\sqrt{\psi} \simeq 1.2\omega_b$. This overstable mode, not
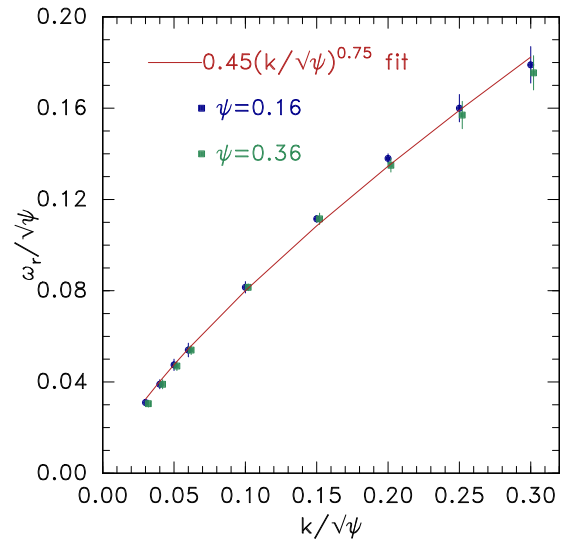

FIG. 4. Relation between oscillation frequency ω_r and wave number k for overstable modes. Points are derived from numerical evaluation of the dispersion relation. The curve is an empirical approximate fit to the points.

considered in the previous analysis, explains why instability and subsequent hole decay is observed in simulations above the previous pure-growth threshold.

IV. TWO-DIMENSIONAL PIC SIMULATIONS

Particle-in-cell simulations were carried out with the code COPTIC [32,33] to compare with the analytic results. The potential is represented on a periodic two dimensional domain $-32 < z < 32$ (trapping direction), $-64 < y < 64$ (transverse direction), and initialized with a $\phi_0 = \psi \, \text{sech}^4(z/4)$ hole uniform in the y direction by seeding the self-consistent particle distribution calculated by the integral equation method [4]. Ions are a uniform immobile background. In total 0.8 billion electron particles on 512 parallel cpus are pushed with a time step of 0.5 (ω_p^{-1}), and cell size 0.5×1 (λ_D) until instability growth is observed. All three electron velocity components are tracked and the particle positions are also periodic.

It is convenient to Fourier transform the resulting potential perturbations in the y direction, so that $\phi(y, z, t) = \sum_\ell A_\ell(z, t) e^{ik_\ell y}$. Mode 0 ($k = 0$) is then the mean, which is essentially the equilibrium in the linear growth phase. The higher modes, ℓ, are the possible periodic eigenmodes $k = k_\ell = 2\pi\ell/128$. The modes' z variation is retained and so each mode depends on time t and position z. Generally a dominant integer mode number is observed to grow, together with adjacent mode numbers of lower amplitude (and different frequency).

Figure 5 shows example contour plots of the dominant mode evolution. Only positions $-10 < z < 10$ close to the hole are shown. Also, although some simulations at late times show strongly nonlinear behavior, that part of the contour part is not displayed since the concern in this paper is only the linear growth phase. The segment of the plot prior to time 20 (where there is no significant perturbation yet) has been replaced with a template that represents an arbitrarily scaled version of the shift mode $-\frac{\partial \phi_0}{\partial z}$ to compare with the later observed structures. Figure 5(a) has a magnetic field strength $\Omega = 0.20$, just below what is needed to stabilize the purely growing mode. It grows without oscillations during the linear phase. Figure 5(b) has $\Omega = 0.25$ in which the purely growing mode has disappeared and an overstable mode with $\ell = 2$ has replaced it. Both these panels have mode positional structure similar to the shift mode. Panel (c) is at $\Omega = 0.45$, the uppermost value of this overstable mode series. It has a much higher mode number: $\ell = 6$. It can also be observed that the z extent of mode (c) is substantially reduced. Its amplitude decreases to *zero* at a position that is near the *peak* of the shift-mode template, with only a small perturbation of reversed polarity outside it. The eigenmode structure is nearly a factor of 2 narrower in z than the shift-mode template.

We obtain from many simulations' mode results like these the real and imaginary parts of the mode frequency ω_r and ω_i, and the dominant k during the linear growth phase. Figure 6 shows the normalized frequencies as a function of normalized field. Analytic predictions of regions are indicated, separated by the analytic stability thresholds for suppression of the purely growing mode $\Omega/\sqrt{\psi} = 0.34$, and the overstable mode $\Omega/\sqrt{\psi} = 0.6$. The normalization by $\sqrt{\psi}$ brings the
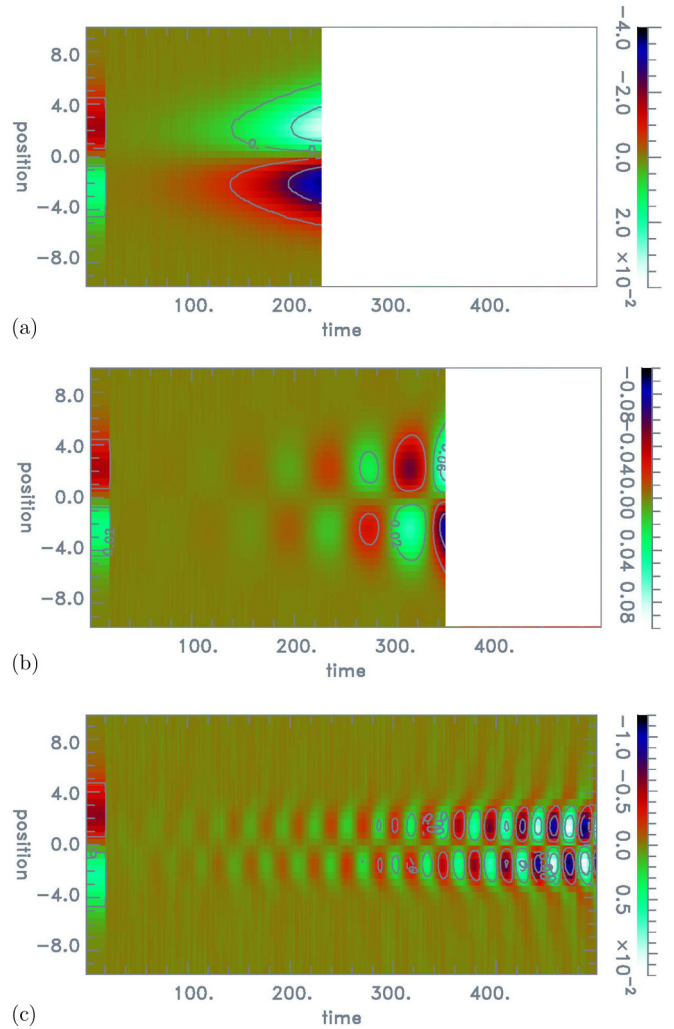

FIG. 5. Examples of unstable potential modes in hole simulations with $\psi = 0.49$. (a) $\Omega = 0.2$, $\ell = 1$, purely growing. (b) $\Omega = 0.25$, $\ell = 2$, oscillatory. (c) $\Omega = 0.45$, $\ell = 6$, oscillatory. The left-hand section $0 < t < 20$ is replaced by the shift mode z profile for comparison with the PIC results. The color bars at right indicate mode amplitudes A_ℓ. Only times prior to the onset of strongly nonlinear behavior are displayed.

points representing PIC results for different ψ into approximately universal curves. The overstable analytic growth rate $\omega_i/\sqrt{\psi} = 0.025$ is shown by the horizontal dash-dot line. It is in good agreement with the observed PIC growth rates (filled points). The transition between pure growth and overstability lies between the lowest two Ω values for each ψ and is in good agreement with the analytic prediction (dashed line). However, the overstable oscillations persist somewhat above the predicted analytic threshold of stability (short-dashed line). In this right-hand region, the growth rate falls until it reaches (near) zero when Ω is 20–25% past the 0.6 threshold.

The real frequency ω_r is shown by open points. The comparison with the fit (7) to analytic results is provided by the single numerals (denoting the observed ℓ), placed at the predicted frequency for that ℓ value. The predictions expected to agree with PIC observations are joined to the observed ω_r by vertical lines, whose relative shortness shows they
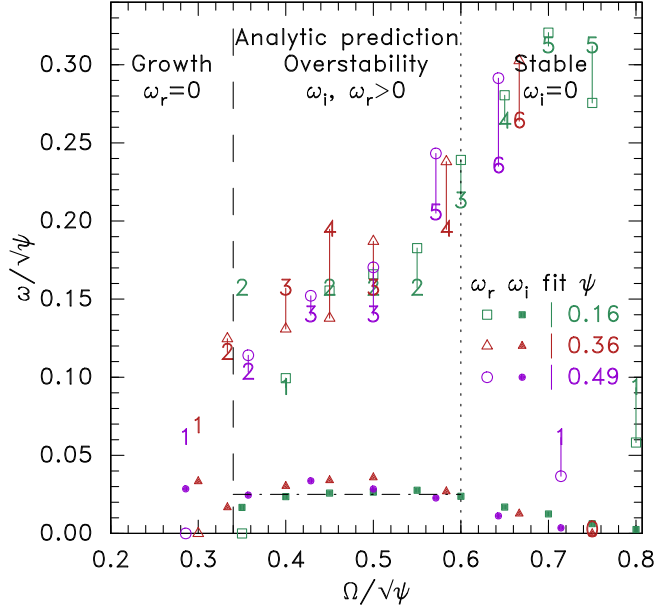
FIG. 6. Simulation observations of unstable real (open points) and imaginary (filled points) frequencies as a function of magnetic field strength. Analytic predictions are shown by dashed lines separating the three Ω regions and showing the growth rate of overstability. Single numerals, denoting the mode number ℓ are placed at the predicted real analytic frequency fit Eq. (7) for the dominant k observed. When the real frequency is nonzero, they are joined by vertical lines to the corresponding frequency ω_r observed in the simulation, to show the degree of agreement.

do indeed fit the observed frequencies well, considering the discreteness of k enforced by the finite y extent. The lowest-Ω (unconnected) points correspond to zero frequency purely growing modes, so they do not fit. The highest-Ω cases show a sudden jump down to $\ell = 1$, and hence much decreased
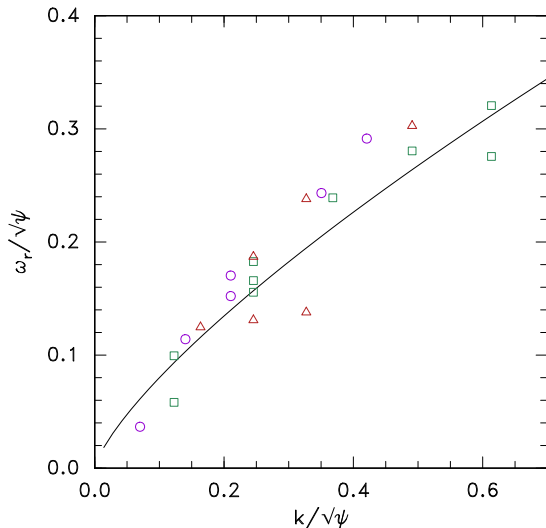

FIG. 7. Comparison of the real frequency dependence on k observed in PIC simulations (points with the same coding as Fig. 6) with the fit (line) of Eq. (7): $\omega_r/\sqrt{\psi} \simeq 0.45(k/\sqrt{\psi})^{0.75}$.

ω_r. They have extremely low ω_i and are effectively stable in respect to the modes treated here analytically.

In Fig. 7 is shown more directly a plot of all the nonzero normalized real frequencies ω_r in the PIC simulations versus their normalized k. They agree well, within the uncertainties of the simulations, with the scaling fit to the analytic results. As Figs. 3 and 6 indicate, there is no simple systematic scaling of the growth rate ω_i with k.

V. DISCUSSION

In summary, the magnetic field suppression of the purely growing instability of electron holes occurs in PIC simulations at a value of cyclotron frequency $\Omega = 0.34\sqrt{\psi}\,\omega_p$ in good agreement with shift-mode analytic theory. That theory, extended to account for oscillatory modes, also agrees well with the real and imaginary parts of observed frequency in the overstable regime. However, the overstability in simulation persists 20–25% beyond the $\Omega \simeq 0.6\sqrt{\psi}\,\omega_p$ at which the shift mode becomes analytically stable. Spatial narrowing of the eigenmode compared with the assumed shift mode appears to be the reason. Deviation from shift mode may also explain the fact that no stable region is observed in simulations between the pure-growth and overstable regions.

The instability of the high-frequency overstable modes into the region above the threshold of stability of the shift-mode analytic calculation can be understood qualitatively as permitted by the reduction of the z width of the actual unstable modes relative to the shift-mode shape. In Ref. [27] it was shown that magnetic field stabilization of the shift mode arises because for cyclotron harmonic $|m| = 1$ the contributions from Φ_m to the trapped particle momentum change their sign across the resonance $m\Omega + \omega = \omega_{\text{bounce}}$, where ω_{bounce} is a function of the trapped particle total energy ($W_\parallel$), that is, of the particle depth in the potential energy well. For a given value of $m\Omega + \omega$, particles bouncing slower than this frequency do not contribute destabilizing trapped momentum. As $m\Omega + \omega$ increases and more trapped particles cease contributing, eventually the balance between trapped and passing momentum jetting is broken by this exclusion and the instability is suppressed. However, the exact value of Ω at which full suppression occurs depends on the z extent of the eigenmode as well as on ω. A narrower-z eigenmode can substantially decrease the momentum perturbation contribution from shallowly trapped and passing electrons, whose orbits extend past the narrow eigenmode, while decreasing little the contribution from deeply trapped particles, whose orbits do not. This effect thus tends to make narrower eigenmodes more unstable than the shift mode. So they can persist at magnetic fields beyond the shift-mode threshold. This sort of consideration also helps explain qualitatively why oscillatory modes are unstable at higher Ω than modes of lower (or zero) ω_r. Instability is driven by particles and m satisfying $|m\Omega + \omega| < \omega_{\text{bounce}}$. The lowest values of $|m\Omega + \omega|$ occur for $m = -1$ and *highest* ω_r; so higher ω_r is liable to be more unstable because more particles contribute to unstable trapped momentum jetting.

Although using the Rayleigh quotient (total momentum conservation) minimizes the dependence of the eigenvalue on the assumed shape of the eigenmode, it does not suppress it

entirely, especially when the deviation from the shift mode is large. The present comparison shows that the shift-mode assumption becomes quantitatively inadequate at high magnetic field. The plasma always finds the most unstable mode, and the shift mode is no longer exactly it.

The eigenmode structure of the coupled hole-wave (streak or whistler) instability observed in simulations at even higher magnetic fields, but unexplored here, deviates from the shift-mode assumption in a different way. The shift mode presumes there is no net potential difference across the hole; the wave coupling violates that assumption. The hole-wave instability might therefore require a more complex eigenmode for its analysis, involving the ingredients described in Ref. [28]. However, a more detailed analysis using the present techniques for the pure shift mode has discovered some oscillatory modes with growth rates typically about 50 times smaller than those found here, at effectively infinite B field. They may prove to be the simulations' hole-wave instability. This topic will be reported elsewhere.

[1] V. A. Turikov, Electron phase space holes as localized BGK solutions, Phys. Scr. **30**, 73 (1984).

[2] H. Schamel, Electrostatic phase space structures in theory and experiment, Phys. Rep. **140**, 161 (1986).

[3] B. Eliasson and P. K. Shukla, Formation and dynamics of coherent structures involving phase-space vortices in plasmas, Phys. Rep. **422**, 225 (2006).

[4] I. H. Hutchinson, Electron holes in phase space: What they are and why they matter, Phys. Plasmas **24**, 055601 (2017).

[5] H. Matsumoto, H. Kojima, T. Miyatake, Y. Omura, M. Okada, I. Nagano, and M. Tsutsui, Electrostatic solitary waves (ESW) in the magnetotail: BEN wave forms observed by GEOTAIL, Geophys. Res. Lett. **21**, 2915 (1994).

[6] R. E. Ergun, C. W. Carlson, J. P. McFadden, F. S. Mozer, L. Muschietti, I. Roth, and R. J. Strangeway, Debye-Scale Plasma Structures Associated with Magnetic-Field-Aligned Electric Fields, Phys. Rev. Lett. **81**, 826 (1998).

[7] S. D. Bale, P. J. Kellogg, D. E. Larsen, R. P. Lin, K. Goetz, and R. P. Lepping, Bipolar electrostatic structures in the shock transition region: Evidence of electron phase space holes, Geophys. Res. Lett. **25**, 2929 (1998).

[8] A. Mangeney, C. Salem, C. Lacombe, J.-L. Bougeret, C. Perche, R. Manning, P. J. Kellogg, K. Goetz, S. J. Monson, and J.-M. Bosqued, WIND observations of coherent electrostatic waves in the solar wind, Ann. Geophys. **17**, 307 (1999).

[9] J. S. Pickett, L.-J. Chen, R. L. Mutel, I. W. Christopher, O. Santolk, G. S. Lakhina, S. V. Singh, R. V. Reddy, D. A. Gurnett, B. T. Tsurutani, E. Lucek, and B. Lavraud, Furthering our understanding of electrostatic solitary waves through Cluster multispacecraft observations and theory, Adv. Space Res. **41**, 1666 (2008).

[10] L. Andersson, R. E. Ergun, J. Tao, A. Roux, O. LeContel, V. Angelopoulos, J. Bonnell, J. P. McFadden, D. E. Larson, S. Eriksson, T. Johansson, C. M. Cully, D. L. Newman, M. V. Goldman, K. H. Glassmeier, and W. Baumjohann, New Features of Electron Phase Space Holes Observed by the THEMIS Mission, Phys. Rev. Lett. **102**, 225004 (2009).

[11] L. B. Wilson, C. A. Cattell, P. J. Kellogg, K. Goetz, K. Kersten, J. C. Kasper, A. Szabo, and M. Wilber, Large-amplitude electrostatic waves observed at a supercritical interplanetary shock, J. Geophys. Res.: Space Phys. **115**, A12104 (2010).

[12] D. M. Malaspina, D. L. Newman, L. B. Willson, K. Goetz, P. J. Kellogg, and K. Kerstin, Electrostatic solitary waves in the solar wind: Evidence for instability at solar wind current sheets, J. Geophys. Res.: Space Phys. **118**, 591 (2013).

[13] D. M. Malaspina, L. Andersson, R. E. Ergun, J. R. Wygant, J. W. Bonnell, C. Kletzing, G. D. Reeves, R. M. Skoug, and B. A. Larsen, Nonlinear electric field structures in the inner magnetosphere, Geophys. Res. Lett. **41**, 5693 (2014).

[14] I. Y. Vasko, O. V. Agapitov, F. Mozer, A. V. Artemyev, and D. Jovanovic, Magnetic field depression within electron holes, Geophys. Res. Lett. **42**, 2123 (2015).

[15] F. S. Mozer, O. A. Agapitov, A. Artemyev, J. L. Burch, R. E. Ergun, B. L. Giles, D. Mourenas, R. B. Torbert, T. D. Phan, and I. Vasko, Magnetospheric Multiscale Satellite Observations of Parallel Electron Acceleration in Magnetic Field Reconnection by Fermi Reflection from Time Domain Structures, Phys. Rev. Lett. **116**, 145101 (2016).

[16] I. H. Hutchinson and D. M. Malaspina, Prediction and observation of electron instabilities and phase space holes concentrated in the lunar plasma wake, Geophys. Res. Lett. **45**, 3838 (2018).

[17] F. S. Mozer, O. V. Agapitov, B. Giles, and I. Vasko, Direct Observation of Electron Distributions inside Millisecond Duration Electron Holes, Phys. Rev. Lett. **121**, 135102 (2018).

[18] F. Mottez, S. Perraut, A. Roux, and P. Louarn, Coherent structures in the magnetotail triggered by counterstreaming electron beams, J. Geophys. Res. **102**, 11399 (1997).

[19] T. Miyake, Y. Omura, H. Matsumoto, and H. Kojima, Two-dimensional computer simulations of electrostatic solitary waves observed by Geotail spacecraft, J. Geophys. Res. **103**, 11841 (1998).

[20] M. V. Goldman, M. M. Oppenheim, and D. L. Newman, Nonlinear two-stream instabilities as an explanation for auroral bipolar wave structures, Geophys. Res. Lett. **26**, 1821 (1999).

[21] M. Oppenheim, D. L. Newman, and M. V. Goldman, Evolution of Electron Phase-Space Holes in a 2D Magnetized Plasma, Phys. Rev. Lett. **83**, 2344 (1999).

[22] L. Muschietti, I. Roth, C. W. Carlson, and R. E. Ergun, Transverse Instability of Magnetized Electron Holes, Phys. Rev. Lett. **85**, 94 (2000).

[23] M. M. Oppenheim, G. Vetoulis, D. L. Newman, and M. V. Goldman, Evolution of electron phase-space holes in 3D, Geophys. Res. Lett. **28**, 1891 (2001).

[24] N. Singh, S. M. Loo, and B. E. Wells, Electron hole structure and its stability depending on plasma magnetization, J. Geophys. Res. **106**, 21183 (2001).

[25] Q. M. Lu, B. Lembege, J. B. Tao, and S. Wang, Perpendicular electric field in two-dimensional electron phase-holes: A parameter study, J. Geophys. Res. **113**, A11219 (2008).

[26] I. H. Hutchinson, Kinematic Mechanism of Plasma Electron Hole Transverse Instability, Phys. Rev. Lett. **120**, 205101 (2018).

[27] I. H. Hutchinson, Transverse instability of electron phase-space holes in multi-dimensional Maxwellian plasmas, J. Plasma Phys. **84**, 905840411 (2018).

[28] D. L. Newman, M. V. Goldman, M. Spector, and F. Perez, Dynamics and Instability of Electron Phase-Space Tubes, Phys. Rev. Lett. **86**, 1239 (2001).

[29] M. Berthomier, L. Muschietti, J. W. Bonnell, I. Roth, and C. W. Carlson, Interaction between electrostatic whistlers and electron holes in the auroral region, J. Geophys. Res.: Space Phys. **107**, SMP 26-1 (2002).

[30] M. Wu, Q. Lu, C. Huang, and S. Wang, Transverse instability and perpendicular electric field in two-dimensional electron phase-space holes, J. Geophys. Res.: Space Phys. **115**, A10245 (2010).

[31] B. N. Parlett, The Rayleigh Quotient Iteration and Some Generalizations for Nonnormal Matrices, Math. Comput. **28**, 679 (1974).

[32] I. H. Hutchinson, Nonlinear collisionless plasma wakes of small particles, Phys. Plasmas **18**, 032111 (2011).

[33] Available from https://github.com/ihutch/COPTIC